



Environmental Sensing in Existing Fiber Networks

Muhammad Nazri Bin Nordin

Supervised by Christian Kurtsiefer

A thesis submitted for the degree of
Bachelor of Science with Honours in Physics

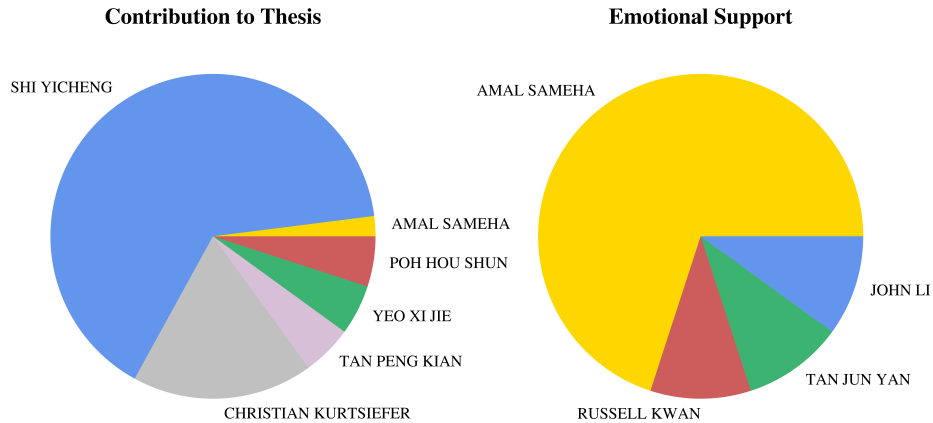
Department of Physics
National University of Singapore

2021

This Honours Thesis represents my own work and due acknowledgement is given whenever information is derived from other sources. No part of this Honours Thesis has been or is being concurrently submitted for any other qualification at any other university.

Signed: _____

Acknowledgement



First, I would like to thank Prof. Christian KurtSiefer for giving me the opportunity to work on such an exciting project.

Next, I would like to express my most sincere gratitude to my mentor, Shi YiCheng, who in months' time I shall address as Dr. Shi. Your guidance, patience and occasional humour were instrumental to my fulfilling FYP journey.

A special mention goes to Tan Peng Kian, Yeo Xi Jie and Poh Hou Shun for providing extremely useful insights, and for helping me through dry runs.

To John Li, Russell Kwan and *Tan* Jun Yan, thank you for being by my side throughout my undergraduate years.

And of course, to Amal Sameha, thank you for not only being my pillar of support, but also for helping me interpret the data I processed throughout my FYP.

Abstract

Present-day underwater earthquake sensors like ocean bottom seismometers require a high cost to build and deploy. Installing existing submarine fibers into an interferometer is, on the other hand, a cost-effective alternative. This thesis therefore aims to describe the development of a fiber-based Michelson interferometer that is able to sense mechanical perturbations in the environment. This is done by measuring phase changes induced in the fibers as a result of the perturbations. In addition, by interfering two light fields of different frequencies, one can convert the Michelson interferometer into a heterodyne phasemeter, which is able to measure phase changes without any direction ambiguity.

Contents

Acknowledgement	v
Abstract	vii
1 Introduction	1
1.1 Earthquakes	1
1.2 Existing Efforts in Underwater Earthquake Detection	2
1.3 Thesis Outline	4
2 Building a Fiber-Based Michelson Interferometer	5
2.1 Michelson Interferometry	5
2.2 Experimental Setup	10
2.3 Influence of Phase Noise From Laser	11
2.4 Perturbation Sensing in Lab	17
2.5 Perturbation Sensing in Building	19
2.6 Why Michelson Interferometry	22
3 Converting into a Heterodyne Phasemeter	25
3.1 Heterodyning the Setup	26
3.2 Perturbation Sensing in Lab	29
4 Conclusion and Outlook	31
Bibliography	33

1 Introduction

1.1 Earthquakes

Natural disasters cause an average of 60,000 deaths and more than US\$50 billion in economic loss every year throughout the world [1, 2]. Between 2000 and 2019, 4 out of the 5 deadliest natural disasters that happened were due to earthquakes [3].

Table 1.1: Death toll and the economic cost of the five deadliest natural disasters between 2000 and 2019 [3–7].

Natural Disaster	Location	Year	Deaths	Cost (US\$)
Sumatra–Andaman earthquake	Indian Ocean	2004	226,408	14 billion
2010 Haiti earthquake	Haiti	2010	222,570	8 billion
Cyclone Nargis	Myanmar	2008	138,366	12 billion
Great Sichuan earthquake	China	2008	87,476	120 billion
2005 Kashmir earthquake	Pakistan	2005	73,338	5.2 billion

Earthquakes are associated with sudden shaking of the Earth caused by tectonic shifts, volcanic eruptions, or man-made explosions, leading to release of strain energy stored in rocks in the form of seismic waves [8, 9]. There are several types of seismic waves, often classified as body waves and surface waves [10]. Body waves are named *body* waves since they travel through the interior of Earth, and the two types are Primary waves (P-waves) and Secondary waves (S-waves) [11]. On the other hand, Rayleigh waves, Love waves and Stoneley waves are called surface waves as they travel along the Earth’s surface [11].

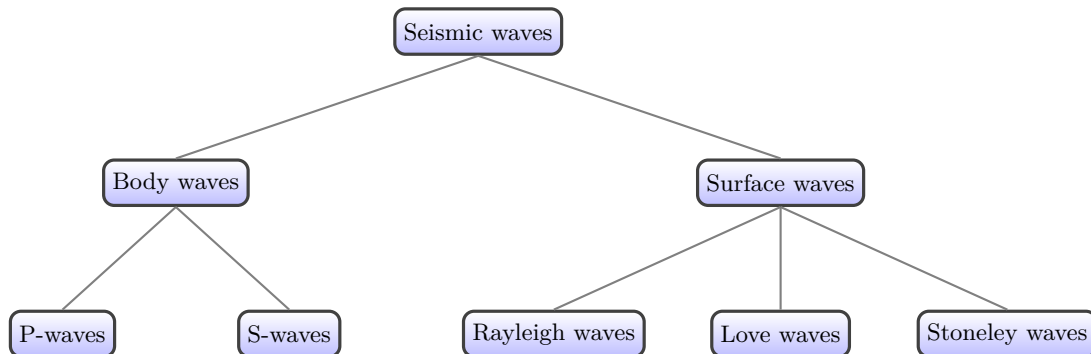


Figure 1.1: Classification of seismic waves.

The strength of an earthquake is classified using various magnitude scales such as the *Richter* scale, denoted by M_L , and the moment magnitude scale, denoted by M_W [12]. The

latter is usually preferred as it is the only physically well defined, non-saturating magnitude scale for earthquakes [13]. Using the 4 earthquakes in Table 1.1 as examples, the moment magnitudes for the Sumatra–Andaman earthquake, 2010 Haiti earthquake, Great Sichuan earthquake and 2005 Kashmir earthquake had moment magnitudes of M_W 9.0, M_W 7.0, M_W 7.9 and M_W 7.6 respectively [4, 14–16].

The Sumatra–Andaman earthquake started off as an earthquake, but most of the destruction to life and property was caused by the resulting *tsunami* - which means *harbour wave* in Japanese - that reached 30 m in height [4, 17]. The damage unfolded from the tsunami was more significant as there were no proper alert systems at the time [18]. When the seismic event was detected by the United States (US), warning could not be delivered to Indonesian officials as they were not contactable, despite numerous attempts [19]. Thus, to minimise the extent of damage to life and property by earthquakes and tsunamis, earthquake detection is important everywhere in the world - in both land and water. After all, no part of the world is immune to earthquakes, although most are concentrated on the continental plate boundaries, called the *Ring of Fire* [20]. Indonesia, Japan and US are three of the many countries located along the Ring of Fire.

1.2 Existing Efforts in Underwater Earthquake Detection

Even though 70% of the surface of the Earth is water, almost all seismic stations are on land (e.g. GB.SWN1, GB.HMNX, MN.WDD), and these stations use seismometers [21–23].

A seismometer is based on inertial-pendulum systems. It consists of a ballast mass attached to a spring, and the other end of the spring is attached to a frame that is fixed to the ground. During an earthquake, the frame moves. On the other hand, the mass does not move due to its large inertia. The motion of the frame with respect to the mass is transformed into an electrical voltage which is recorded. The recorded voltage is proportional to the motion of the mass relative to the Earth from which the absolute motion of the ground can be derived. When detecting earthquakes, both types of body waves - P-waves and S-waves - are detected first since they travel faster than surface waves [24]. P-waves will arrive before S-waves, although the latter causes higher amplitudes of motion [24].

Frequencies of seismic waves lie within the order of tens of Hertz, and the usual frequency detection range for earthquakes is targeted between 0.1 and 20 Hz [25, 26]. The reason for this is that most man-made structures have natural vibration frequencies in this range [25].

Since most seismic stations are on land, underwater earthquakes of $M_W < 4$ therefore remain largely undetected because they are too weak to be measured with land-based seismic stations [26]. To circumvent this, underwater seismic sensors such as ocean bottom seismometers (OBSs), have been deployed at earthquake-prone areas [27, 28]. However, the issue with OBS is that it is costly - building one costs about US\$100,000, five times the cost of its land-based counterpart and deploying it would only drive the price higher [26, 29, 30]. This means that deploying a network of OBSs big enough to cover Earth's waters would be financially impractical to install and maintain.

Alternatively, existing submarine telecommunication fibers could be used as earthquake sensors by building them into an interferometric system. In the oceans, the total length of installed fibers is over 1 million kilometers - if put in a straight line could go around the circumference of the Earth 25 times [31]. Global coverage could be achieved with minimal cost as the need for deployments to the middle of the ocean would be reduced, considering that the system would be accessible from land. With this technique, earthquake detection can be achieved by measuring phase changes of the light propagating in the fiber, due to changes in refractive index when perturbed [26]. Another possible way of achieving earthquake detection with a fiber-based interferometer is by measuring changes in polarisation states in the fiber [32].

Another method of using existing fibers to detect earthquakes is by the distributed acoustic sensing (DAS) technique [33, 34]. The DAS method employs a laser interrogator unit located at one end of the fiber whose purpose is to illuminate the fiber with short pulses and study the Rayleigh backscatter of light. Backscattered photons will return to the interrogator unit at a time proportional to the fiber distance traveled, and the retrieved phase shift is proportional to the change in strain due to the seismic waves [35]. However, the usable range in DAS is less than 100 km [26]. This means that using DAS is not as favorable when compared to using an interferometric system. Detecting earthquakes with submarine fibers of lengths up to 535 km had been achieved with a fiber-based interferometer, more than 5 times the working range of a DAS system [26].

For these considerations, this thesis thus proposes developing a fiber-based interferometric system that can detect mechanical perturbations in the environment. The working principles and advantages of an interferometric system can be better understood in the following chapter.

1.3 Thesis Outline

The purpose of this thesis is to describe the development of a fiber-based interferometric system, called the *heterodyne phasemeter*, that is able to detect mechanical perturbations in the environment. The difference between a phasemeter and an interferometer is the former's additional ability to unwrap phase changes from the output signal without direction ambiguity [36]. The heterodyne phasemeter is able to resolve micrometer-scale length changes in optical path due to mechanical perturbations including, but not limited to, those in the typical earthquake range of 0.1 to 20 Hz. In this thesis, mechanical perturbations are simulated in several ways - by moving a mirror in the setup (i.e. by turning the micrometer screw), human motions (e.g. walking, touching the table) and other typical activities in the lab (e.g. opening the door, opening drawers).

Chapter 2 highlights the modifications to the simple Michelson interferometer, as in Figure 2.1, that allow the setup to detect perturbations in the environment with fibers. Additionally, the limitations of the Michelson interferometer, along with the corresponding adopted solutions will be discussed. The chapter will then end off with 2 applications, the first being the detection of perturbations in the lab and the second being the detection of perturbations in the building, S15 of National University of Singapore (NUS).

Chapter 3 then features the heterodyning process of the setup, resulting in the heterodyne phasemeter. Likewise, its working principles and advantages will be explained, before ending off with a test run to detect perturbations in the lab.

The thesis will be concluded in Chapter 4 in which remarks and outlooks will be provided.

2 Building a Fiber-Based Michelson Interferometer

2.1 Michelson Interferometry

2.1.1 Micrometer Resolution of Interferometric Sensors

Interferometry allows for measurements with resolution in the order of a micron or even smaller [37, 38]. This is possible due to optical interference, a phenomenon in which waves, in our case light, interact and superimpose.

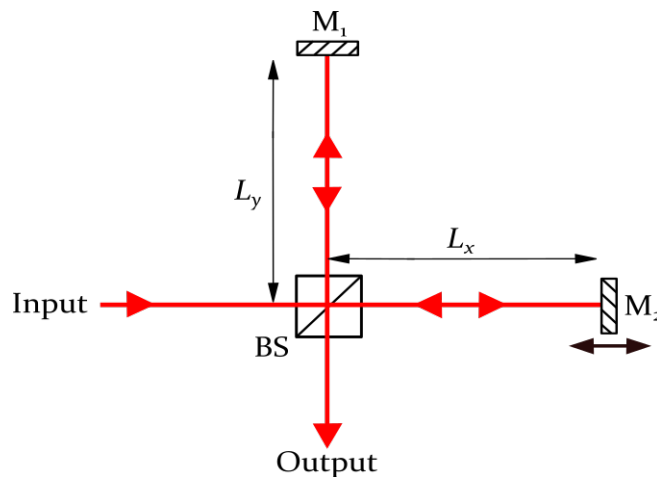


Figure 2.1: The Michelson interferometer. The apparatus consists of a 50:50 beamsplitter (BS) and two mirrors M_1 and M_2 . Interference fringes are observed at the output port as the length of one of the arms (arm 2 in this case) is varied.

The basic principles of interference can be understood by reference to the Michelson interferometer illustrated in Figure 2.1. The simplest version of the Michelson interferometer consists of a 50:50 beamsplitter (BS) and two mirrors M_1 and M_2 . Light is incident on the input port of the BS, where it is divided and directed towards the mirrors. The light reflected off M_1 and M_2 recombines at BS, producing an interference pattern at the output port. The path length of one of the arms can be varied by translating one of the mirrors (assume it is M_2) in the direction parallel to the beam.

Let us assume that the input beam consists of parallel rays from a monochromatic source (e.g. a laser) of wavelength λ and amplitude E_0 . The output field is obtained by summing the two contributions from the waves reflected back from M_1 and M_2 with their phases

determined by the path lengths [36]

$$E_{out} = \frac{1}{2}E_0e^{2ikL_x}(1 + e^{2ik\Delta L}) \quad (2.1)$$

$$= \frac{1}{2}E_0e^{2ikL_x}(1 + e^{i\phi_d}) \quad (2.2)$$

where $k = 2\pi/\lambda$ is the wavenumber of the laser, L_x is the length of arm 2, ΔL is the length difference between the two arms (hence $\Delta L = L_x - L_y$) and $\phi_d = 2k\Delta L$ is the differential phase.

Constructive interference happens when

$$2k\Delta L = 2m\pi, \quad (2.3)$$

and destructive interference happens when

$$2k\Delta L = (2m + 1)\pi, \quad (2.4)$$

where m is an integer. Thus as L_y is scanned, bright and dark fringes appear at the output port with a period equal to $\lambda/2$. The interferometer thus forms a very sensitive device to measure differences in the optical path lengths of the two arms.

In the context of this thesis, the two arms of the interferometer are not air paths, but rather fibers. While the length of the fibers are fixed, changes in optical path lengths in this case is due to changes in the fibers' refractive indices when it is perturbed [39].

2.1.2 Coherent Light Source for Michelson Interferometer

The discussion of the interference pattern in the previous section assumed that the phase shift between the two interfering fields was determined only by the path difference, $2\Delta L$, between the arms. However, this is an idealised scenario that ignores the frequency stability of the light. In realistic sources, the output contains a range $\Delta\omega$ of angular frequencies which leads to the possibility that bright fringes for one frequency occur at the same position as the dark fringes for another [40]. Since this washes out the interference pattern, it is apparent that the frequency spread of the source imposes practical limits on the maximum path difference that will give observable fringes.

Coherence describes the statistical similarity of light at two points in space or time [41].

The two types of coherence are generally distinguished as temporal coherence and spatial coherence, but in this thesis we limit the discussion to temporal coherence as it is the only relevant type here [42].

The temporal coherence of a laser beam is quantified by its coherence time τ_c , where

$$\tau_c = \frac{1}{2\pi\Delta\omega} \quad (2.5)$$

An analogous quantity called the coherence length L_c can be obtained from:

$$L_c = c\tau_c \quad (2.6)$$

The main idea is that for as long as $2\Delta L \leq L_c$, the interference fringes would still be visible, and hence perturbations would still be detectable. Ideally, the chosen light source should have a large L_c , or in other words, the chosen light source should be temporally coherent. An example of a coherent light source is a monochromatic laser with a small linewidth. In our case, the light source used is a 1550 nm laser with a prescribed linewidth of 50 kHz, translating to a coherence length of about 600 m (after taking account the velocity factor of light, 0.659, in a fiber). The choice of wavelength is unrelated to coherence - it is the wavelength that minimises transmission loss in fibers [43].

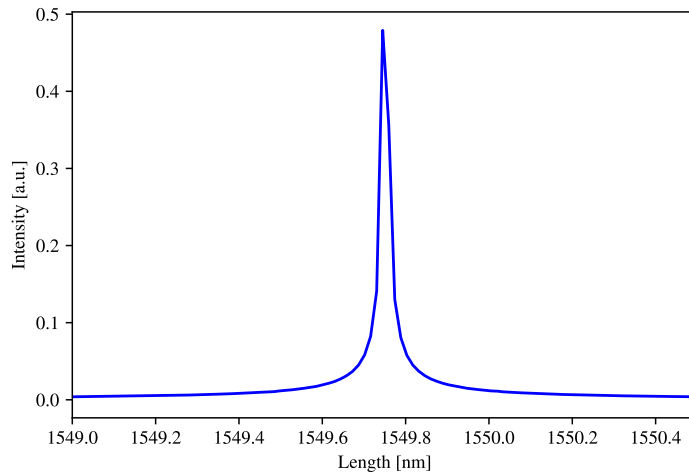


Figure 2.2: Spectrum of SFL1550S Thorlabs external cavity laser with wavelength centered at 1549.75 nm. The spectrum was obtained with a wavemeter with a resolution limit of 3 GHz. The true linewidth of the laser is thus unresolved.

2.1.3 Analysing Output Light

To analyse the resulting interference, if any, the simple Michelson interferometer in Figure 2.1 requires a few necessary components - a detector, a signal analyser (e.g. an oscilloscope) and a pair of collimating lenses. Also, since this thesis aims to develop a fiber-based interferometric system, fibers should be incorporated into its ports, as reflected in Figure 2.3.

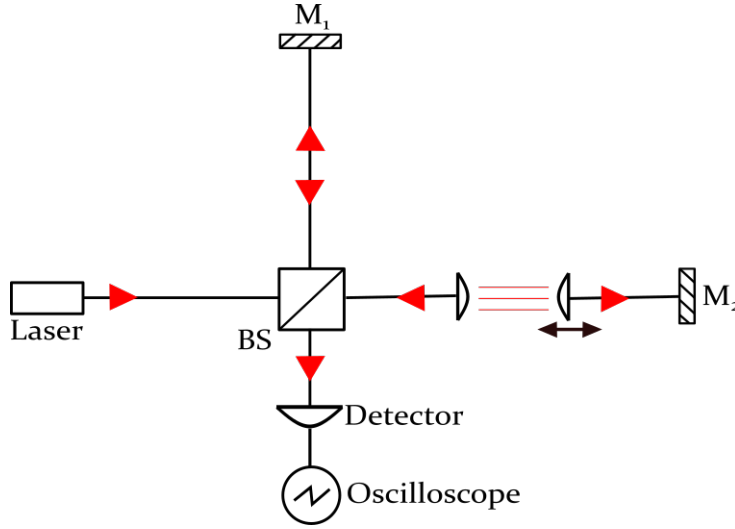


Figure 2.3: All ports of the Michelson interferometer are fibers. Recombined light in the output port propagates towards a photodiode where it is detected, before being analysed in oscilloscope. In arm 2 (or the sensing arm), light is collimated and one of the collimating lens is mounted on a movable stage.

Initially, changes in optical paths can be realised by moving mirror M_2 . However, with the use of fibers in the interferometer, moving M_2 would not result in the same effect as the length of the fiber, and hence the arm length, is fixed. There is a need to collimate the light in arm 2, or what shall be referred to as the sensing arm from here on, and have one of the collimating lens mounted on a movable stage. In our case, the movement of the stage can be controlled with a micrometer screwgauge. This way, the path length of the sensing arm can be similarly varied.

At the output port, the optical power, P_{out} , is given by the mod-square of Equation 2.2 such that

$$P_{out} = \frac{P_{in}}{2} [1 + \cos(\phi_d)]. \quad (2.7)$$

From Equation 2.7, it can be seen that the output power goes between zero and the full input laser power P_{in} , depending on the differential phase ϕ_d . Also, the cosine term implies that when ΔL is varied, the output power is sinusoidal. Equation 2.7 as a function of ϕ_d can be plotted to confirm this behaviour, which is shown as Figure 2.4.

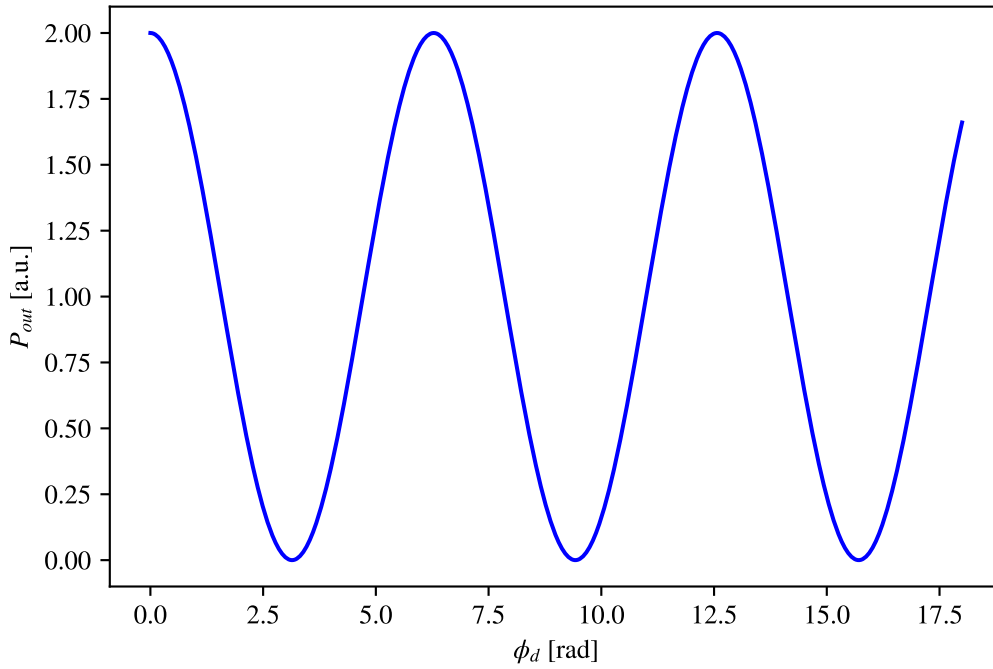


Figure 2.4: Output power of interferometer, P_{out} , varies sinusoidally as ΔL , or ϕ_d , is varied. Graph is obtained by plotting Equation 2.7 as a function of ϕ_d .

The oscilloscope however does not read out P_{out} directly. Instead, it measures variations of voltage proportional to P_{out} over a period of time t . Thus, we should expect that the output signal from the oscilloscope to be a plot of voltage against t .

2.2 Experimental Setup

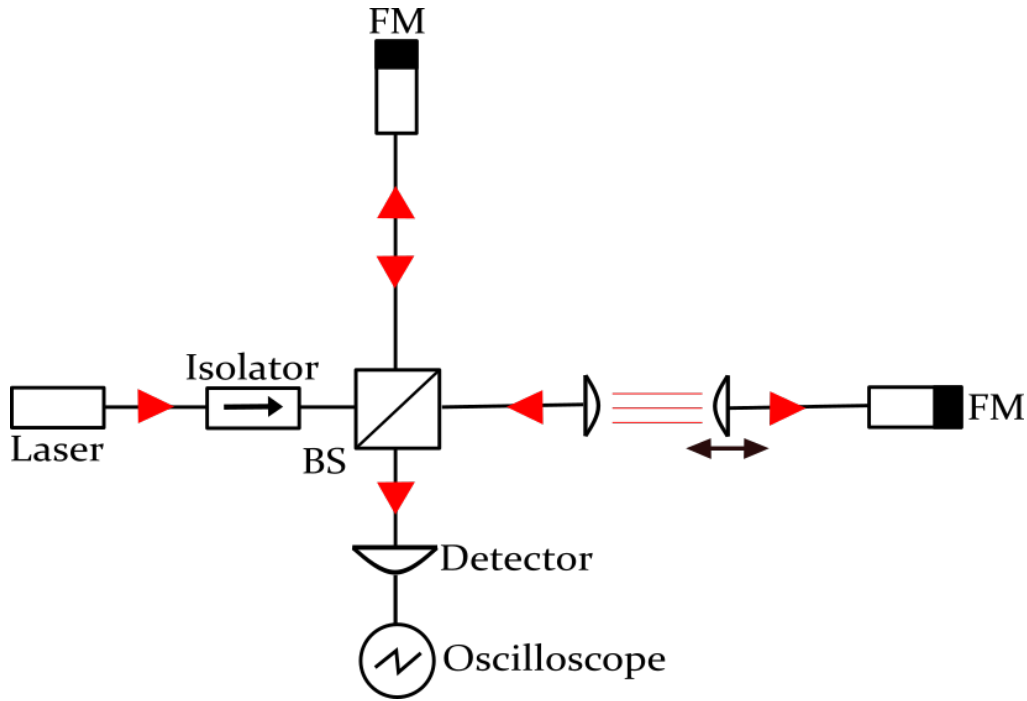


Figure 2.5: Michelson interferometer setup after addition of an isolator and Faraday mirrors (FM).

Figure 2.5 shows the schematic of our Michelson interferometer. An isolator and two Faraday mirrors (FM) are added into the setup.

An isolator is connected after the laser to prevent optical feedback, which happens when light propagates backwards and into the laser. This would induce frequency noise and cause the laser to operate in an unwanted lasing mode, i.e. multi mode instead of single mode (as in Figure 2.2) [44]. Meanwhile, the mirrors are swapped with FMs to eliminate random polarisation states induced in the fibers, which will otherwise degrade the sensitivity of the setup [45]. This is achieved by the Faraday effect - after light reflects off the FM, its polarisation state is shifted by π , i.e. the resulting polarisation state becomes orthogonal to that of the incident light [46].

To test the setup, the knob of the micrometer screwgauge is turned, and the results are shown in Figure 2.6.

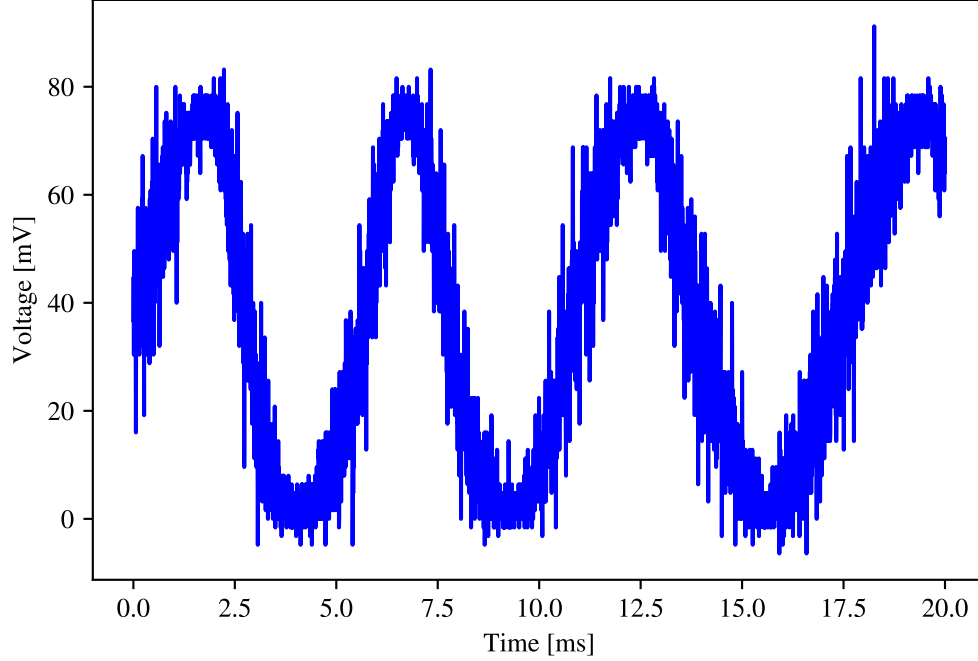


Figure 2.6: A sinusoid is obtained when the knob of micrometer screwgauge in the sensing arm is turned, as predicted in the previous section.

2.3 Influence of Phase Noise From Laser

As mentioned briefly in Subsection 2.1.2, in reality, true monochromatic light does not exist. Frequency fluctuations are often a significant source of noise in many precision interferometry experiments [40], it is useful to investigate how frequency fluctuations couple to the optical phase. We can do so by separating the wavenumber into an average component, k_0 , and a time-fluctuating component, $\delta k = 2\pi\delta f/c$. The length difference is similarly divided into constant, L_0 , and fluctuating δL components. In both cases, the time-fluctuating component is assumed to be much smaller than the constant value. Combining these terms, the differential phase is now

$$\phi_d = 2(k_0 + \delta k)(L_0 + \delta L) \quad (2.8)$$

$$= 2(k_0 L_0 + k_0 \delta L + \delta k L_0). \quad (2.9)$$

The first term is the constant term, or when the length difference is unchanged. The

second term is the interest of this thesis - when the length difference between the two arms is varied, the output power varies sinusoidally. As such, for this we consider that a perturbation is detected. The third term refers to phase noise in the setup due to frequency fluctuations of the laser being coupled to the length difference of the arms, L_0 . This suggests that phase noise will increase when the L_0 increases.

To investigate, a spectrum analyser is used, and the power spectra of the output signal from the photodiode is collected for $L_0 = 0.2\text{ m}$, 6.2 m and 15.2 m .

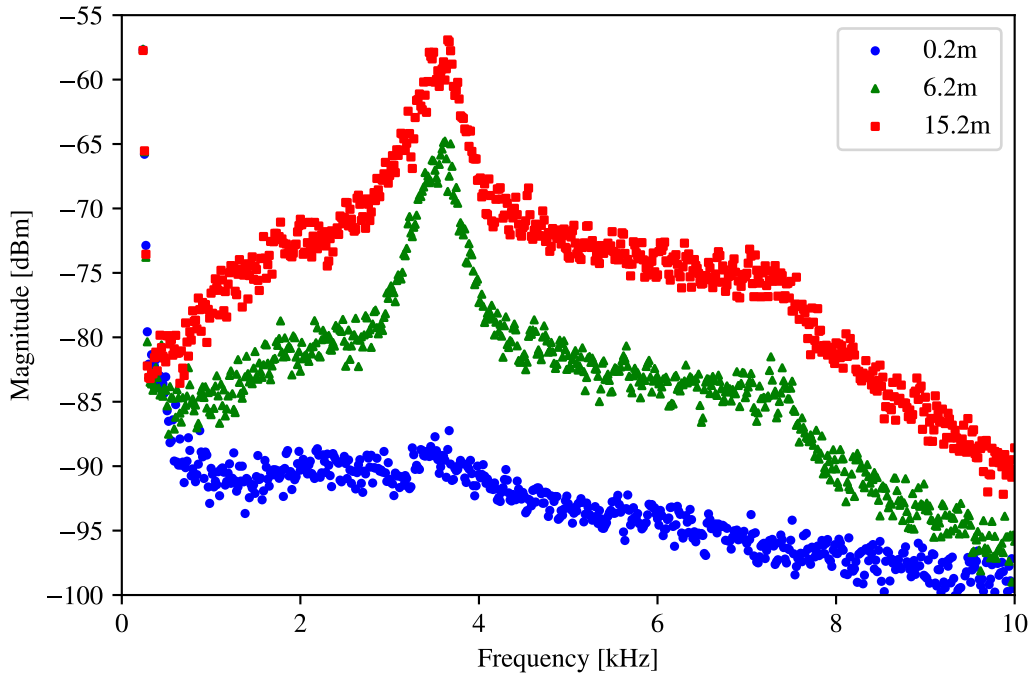


Figure 2.7: Power spectra of output signal from photodiode with different values of L_0 used. As L_0 increases from 0.2 m to 15.2 m , optical power of output signal increases. The peaks near 4 kHz are identified to correspond to mechanical perturbations.

From Figure 2.7, it can be seen immediately that the power of the spectra increases with increasing L_0 . The peak near 4 kHz correspond to the presence of mechanical perturbations when the measurements were made. Mechanical perturbations were simulated by knocking on the table, for example, and a larger increase in power below the 5 kHz range was observed. Since we are interested in investigating the onset of phase noise, we chose 3 frequency values ($f = 5.81\text{ kHz}$, 6.44 kHz and 7 kHz) beyond the range where the mechanical perturbations correspond to (i.e. the flat regime), and plotted a graph of power against L_0 . When

the logarithmic scale is used for both x-axis and y-axis, we found that there is a linear relationship, in agreement with findings by Dandridge et al. [40].

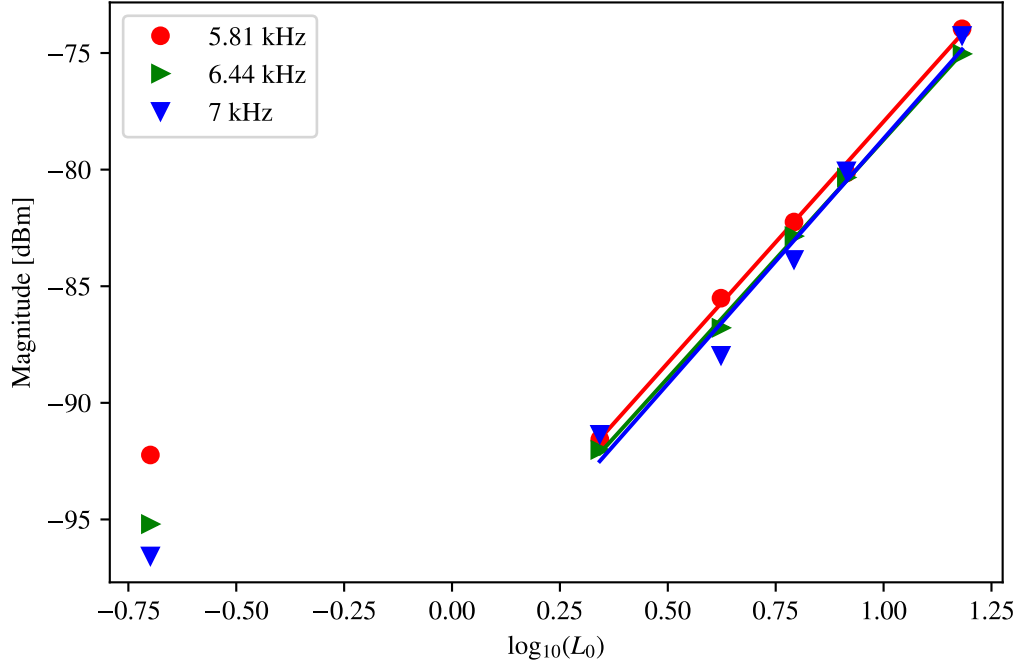


Figure 2.8: As L_0 increases, phase noise increases linearly. The values of L_0 used were $L_0 = 0.2$ m, 2.2 m, 4.2 m, 6.2 m, 8.2 m and 15.2 m. The first data points on the left correspond to baseline noise, present even when L_0 is approximately zero.

This highlights the detrimental effect of the frequency instability of a light source. As mentioned in Subsection 2.1.2, the onset of phase noise will wash away the interference fringes. From Figure 2.8, we can see that the magnitude increased by about 20 dBm, corresponding to a 100 times increase in phase noise, when L_0 is increased by 10 m (comparing the first and last data points along the best fit line).

To tackle this issue, there are 2 possible solutions. The first would be to minimise frequency fluctuations of the laser by using an external cavity like in [26]. However, this would increase the cost of the setup considerably. Alternatively, we can minimise the L_0 at all times so that the phase noise term remains small.

However, while the proposed solution may seem simple, ensuring equal length of fibers in the two arms gets challenging when dealing with longer fibers. It gets even more challenging when the fibers are already set in an infrastructure (e.g. the walls of a building). If the fibers

have been set in concrete for a long period of time, it is possible that the exact length of the fibers become forgotten over time. In that case, measuring the length of the fibers using conventional methods (e.g. measuring tape) is no longer possible. For these considerations, it is imperative to think of an appropriate measuring technique for such circumstances, so as to be able to minimise phase noise when working with any fiber.

2.3.0.1 Minimising Path Difference with Photon Coincidence Method

The photon coincidence method can be employed to measure the length of a physically inaccessible fiber. The setup is given by Figure 2.9 below.

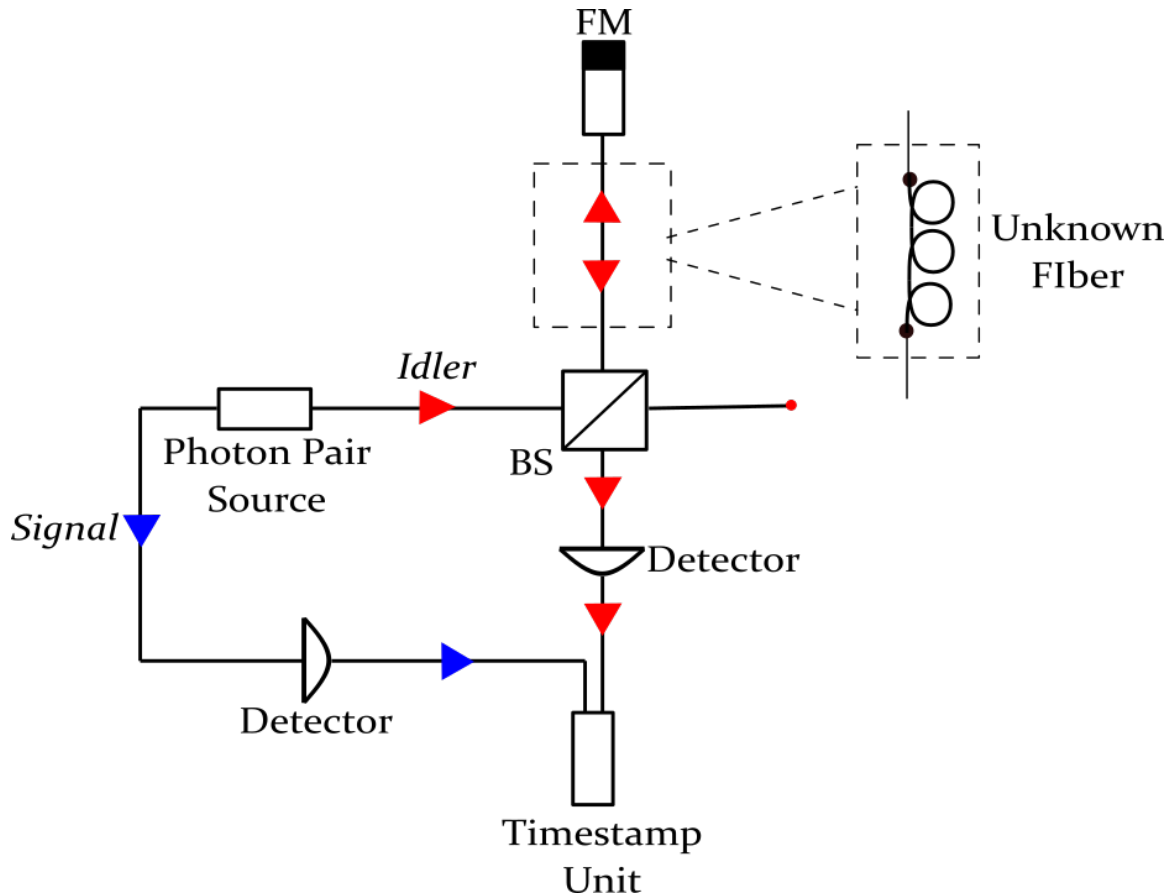


Figure 2.9: Photon coincidence setup to determine length of a physically inaccessible fiber. The photon pair each travels through the signal (blue path) and idler (red path) fiber respectively. Due to the length difference between the signal and idler fibers, there is a time delay τ in the detection of photons in the longer arm.

The photon pair source continuously produces photon pairs within femtoseconds from each other. Each time, the individual photons travels through the signal and idler fibers

respectively. If the signal and idler fibers differ in length, the photon that travels in the longer fiber reaches the timestamp unit later. In other words, a time delay, τ is induced. The length of an unknown fiber can be determined by first plotting coincidence counts against τ . Because the photons travelling in each fiber obeys the same photon statistics, there will be a peak in the coincidence counts graph corresponding to τ .

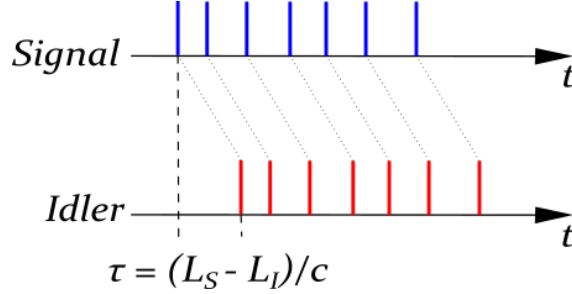


Figure 2.10: A time delay is induced due to difference in length of signal and idler fibers. In this example, the idler fiber is longer.

For our case, the unknown fiber is a building fiber that runs through S15 of NUS, and terminates in the MDF room, behind S15. For ease of monitoring, our interferometer is connected as the idler such that only a FM is required to be connected at the other terminal. Additionally, we require 2 sets of measurements - first by appending a fiber of known length in the idler (i.e. the dotted box in Figure 2.9) and then by connecting the building fiber. This is more convenient as length of signal fiber, as well as other fibers in the setup, are not easily known. With these measurements, the length of the building fiber can then be determined through the following equation

$$\Delta\tau = \frac{L_{known} - L_{building}}{2c/n} \quad (2.10)$$

where $\Delta\tau$ is the difference between the time delays corresponding to the peaks in the respective graphs, L_{known} is the length of the fiber which is known, $L_{building}$ is the length of the building fiber, c is the speed of light and n is the refractive index of the fiber. The factor 2 is included to account for the forward and backward travel path of light in the idler. Alternatively, Equation 2.10 can be rewritten as

$$L_{building} = L_{known} - \frac{2c\Delta\tau}{n}. \quad (2.11)$$

Hence, using $\Delta\tau$ obtained from Figure 2.11, with $L_{known} = 135$ m, $n = 1.467$, $L_{building}$

was computed to be (131.18 ± 0.01) m.

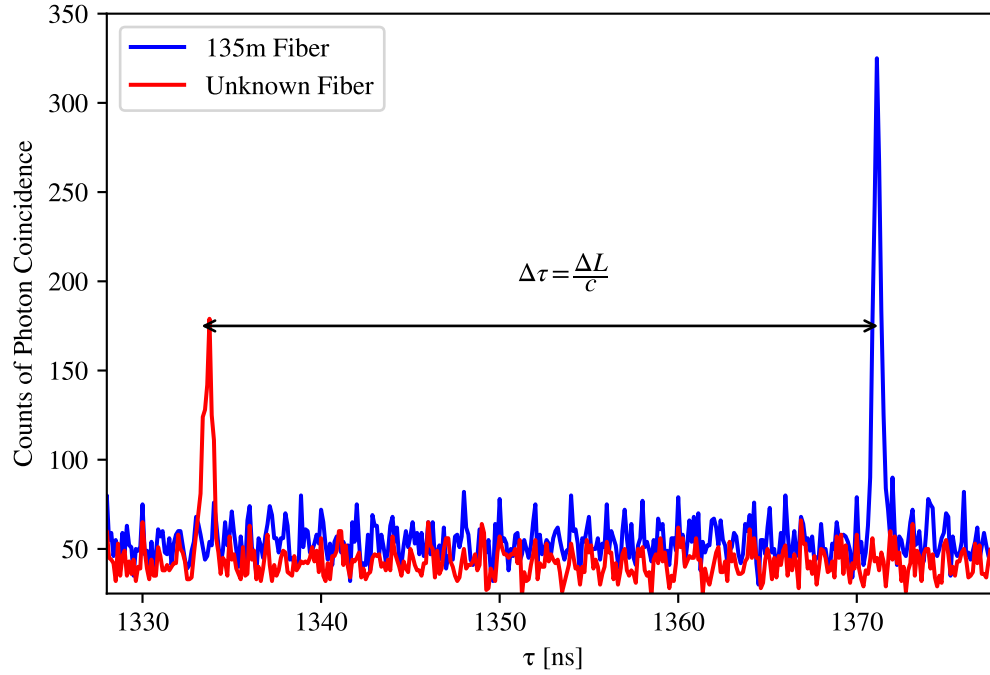


Figure 2.11: Two plots of coincidence counts vs τ were obtained as the length of the signal fiber was also unknown. The length of the building fiber can still be determined by taking 2 sets of measurements - first by using the building fiber, then with a fiber of known length. The length of building fiber is then achieved by finding the difference.

The method can be applied to determine the length of any fiber with centimeter precision, The achieved resolution is better than that of the optical time-domain reflectometry (OTDR), in which recent advancements achieved a resolution of tens of centimeters [47]. However, attention should be given to the coherence length of the source used - the unknown fiber should be shorter than the source's coherence length.

By knowing the length of fibers used, the interferometer arms can be made equal and hence phase noise can be minimised. As a measure of success, a signal trace with low noise should be expected when the inteferometer arms are set to be equal in length. Indeed, this was realised - when the building fiber and a 131 m fiber were connected as the arms of the interferometer (Figure 2.12).

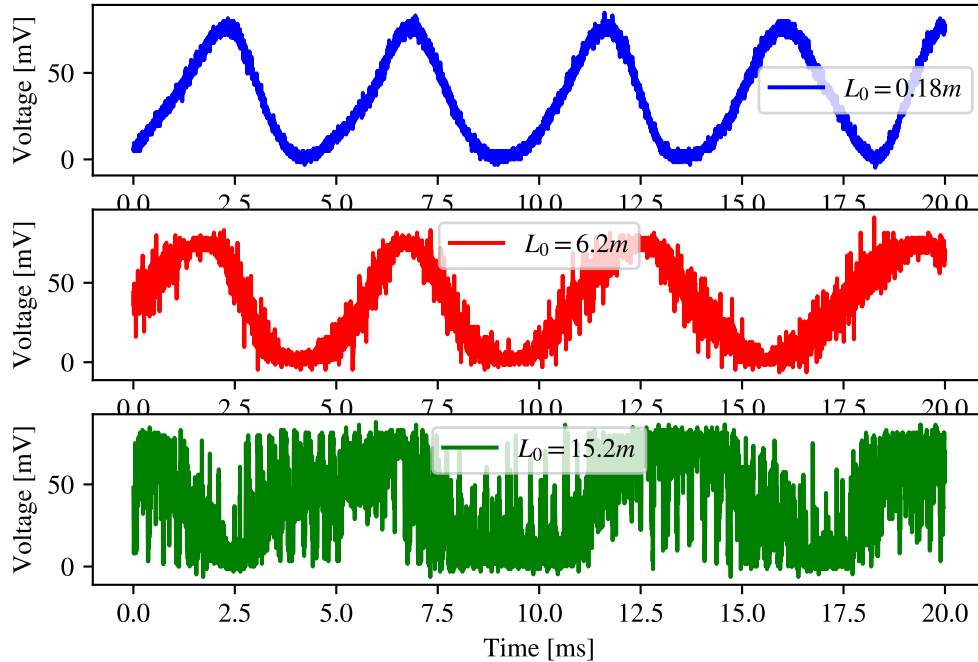


Figure 2.12: A signal trace with low noise after balancing the arms. Here, the sensing arm is the building fiber, and the reference arm is a 131 m fiber, such that $L_0 = 0.18$ m. The bottom 2 graphs, where $L_0 = 6.2$ m and $L_0 = 15.2$ m respectively, are included for bases of comparison.

2.4 Perturbation Sensing in Lab

Nonetheless, we postulate that our Michelson interferometer is be able to detect mechanical perturbations in the environment. In this section, we attempt to do so in a lab setting.

To set an expectation, if the setup works according to the working principles discussed in previous sections, we would be able to observe that there are more perturbations in the lab in the day. The reason for this is that naturally, students and staff in the lab work mostly in the day, hence their movements would be detected by the setup.

2.4.1 Methodology

The setup is given by Figure 2.5, with short fibers of 2 m used in both arms.

A high pass filter was included in the output port, just before the oscilloscope so that the setup only detects sudden and fast fluctuations, while ignoring slowly-drifting baseline

noise of < 1 kHz. The upper bound of the detectable frequency was set by the oscilloscope, at 20 MHz. In other words, the sensing domain of the setup was between 1 kHz and 20 MHz.

The oscilloscope was set in trigger mode, only saving waveforms when there are perturbations in the lab causing the signal amplitude to rise above 12 mV. This value was chosen as it was realized that a 7 dB gain is an acceptable threshold to detect perturbations (after multiple attempts of tapping the table, opening the drawers, opening the lab door, etc.). An example of a triggered signal is illustrated in Figure 2.13. Data was continuously saved over 4 days, before being processed.

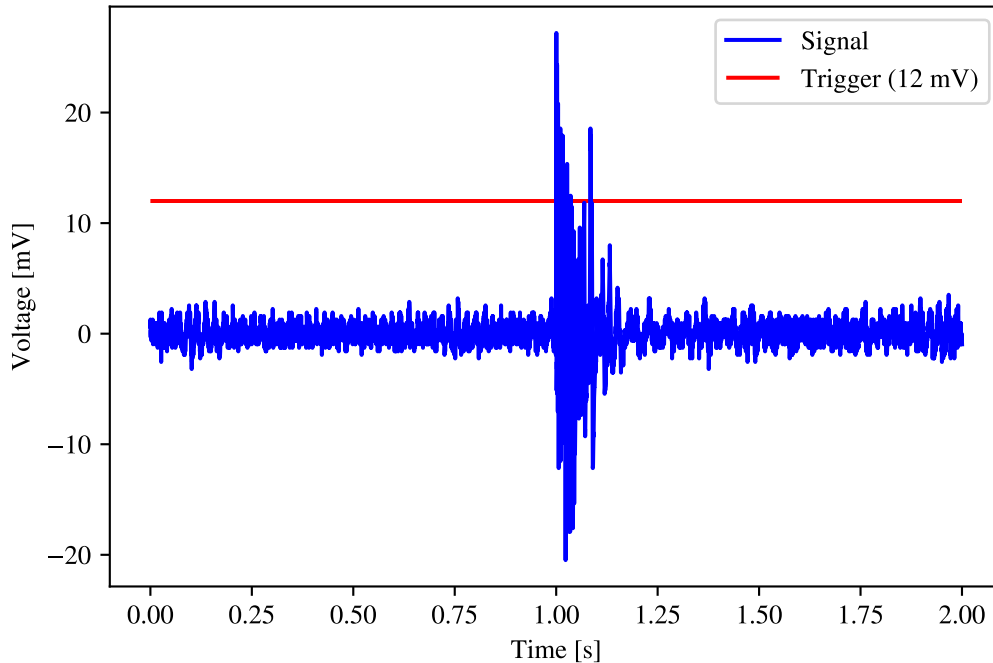


Figure 2.13: A sample waveform that was saved due to perturbations caused by opening the lab door. The maximum signal amplitude exceeds the trigger value of 12 mV.

2.4.2 Results

At the end of the 4 days, a graph of number of traces versus time was plotted (Figure 2.14). As waveforms were only saved when perturbations were detected, given a point of time, the maximum number of traces saved is 1. Hence, greater activity in the lab would be indicated by more densely packed lines.

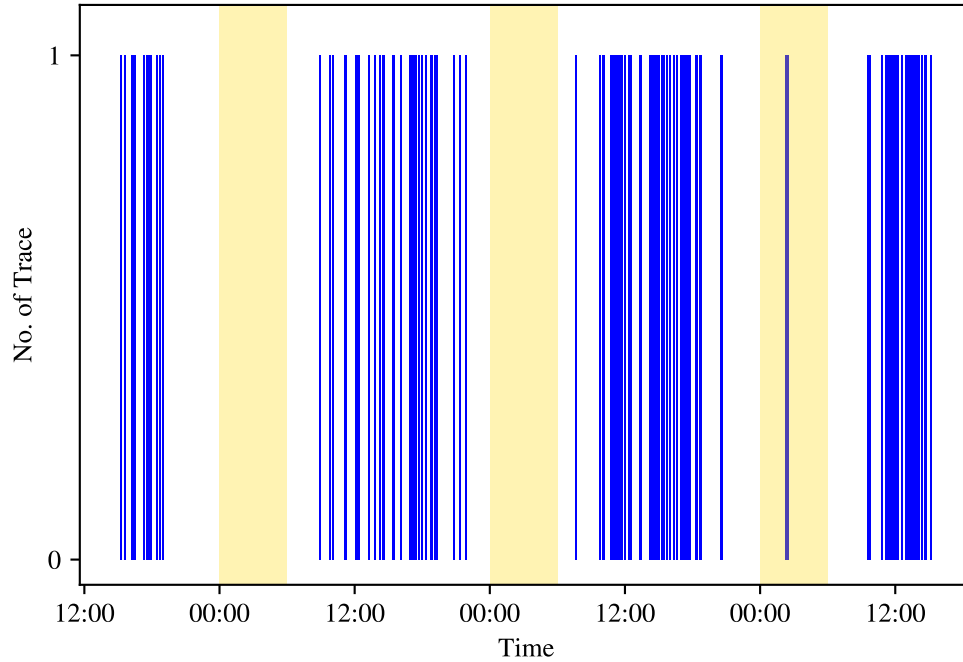


Figure 2.14: A measure of lab activity (23 November 2020, Monday to 26 November 2020, Thursday), shaded regions represent night, which in this case was defined to be the period between 12 am and 6 am.

It is observable that during nighttime, there were hardly any perturbations detected. The exception in the 3rd night was identified - it was caused by one of our group members who entered the lab at 2.30 am. This indicates that our Michelson interferometer setup is able to detect perturbations as our results suggest that it can distinguish between day and night level of activity. Furthermore, it can also distinguish the busyness of the lab across the 4 days, with the busiest day being the 4th day, as the lines were the most closely packed.

2.5 Perturbation Sensing in Building

2.5.1 Methodology

To extend the scale of the previous experiment, we aim to detect perturbations in the building, and so the building fiber was connected in the sensing arm. However, the same data logging and processing methods from before are no longer practical. Since the building fiber extends across the whole of S15, perturbations would always be present, making the trigger method pointless.

Instead, the high pass filter is removed (such that the setup is reverted back into that of Figure 2.5). The oscilloscope is set to save the fast fourier transform (FFT) of the waveforms continuously between 12 pm of 14 January 2021 and 3 am of 15 January 2021. Mechanical perturbations generally have low frequencies within 5 kHz, as identified in Section 2.3. With this consideration, similar to measuring the level of activity in the lab in the previous section, we hope to see that the amplitudes for frequencies in this regime will vary over time as a result of perturbations, with more observable peaks in the day.

2.5.2 Results

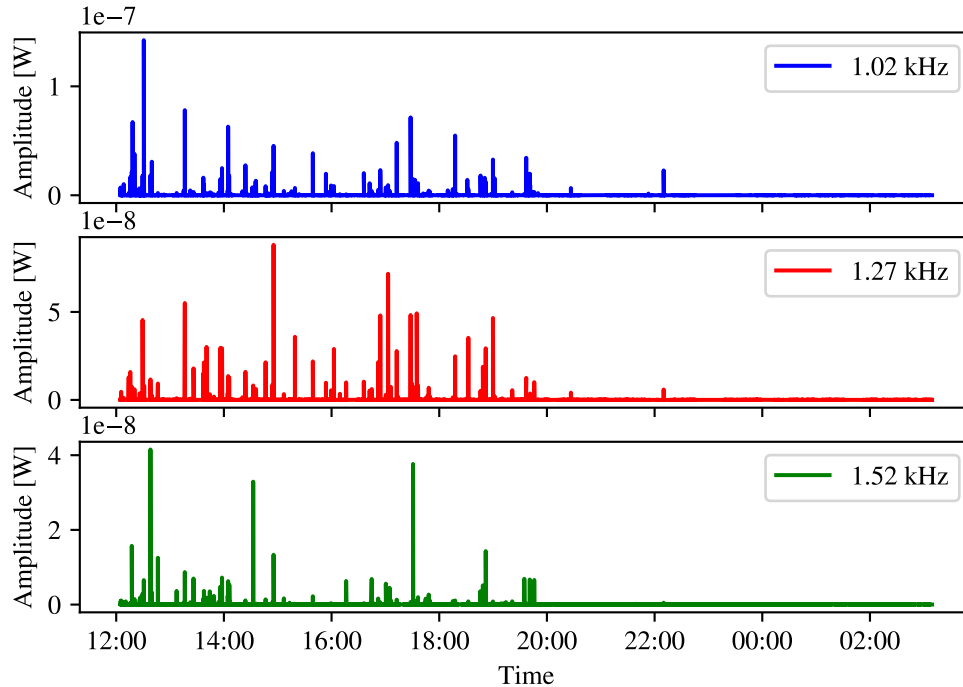


Figure 2.15: A measure of building activity (15 January 2021, Friday to 16 January 2021, Saturday). Our results agree with our expectations: amplitudes of frequencies (e.g. 1.02 kHz, 1.27 kHz and 1.52 kHz) < 5 kHz are high in the day, while low at night.

Indeed, it is observable that in the day, the amplitudes of the frequencies are higher than those at night, suggesting further that our fiber-based interferometer is functioning as intended.

2.5.3 Difference in Temperature Fluctuations

However, since the two arms of the interferometer are in different environments, the temperature fluctuations experienced by the two arms are likely to be different. Hence, it is arguable that the fluctuations in amplitude are due to difference in temperature fluctuations, instead of mechanical perturbations. To investigate the possibility of argument, we perform the following series of calculations.

2.5.3.1 Thermal Expansion of Fibers

For silica, its thermal expansion coefficient is $4.1 \times 10^{-7}/^{\circ}\text{C}$ [48]. Using data from *Weather Underground*, the largest change in temperature on 14 January 2021 is $\Delta T = 2^{\circ}\text{F} = 1.11^{\circ}\text{C}$ which occurred over 30 minutes. Assuming that the entire length of the fiber experiences the same temperature change, for a 131 m fiber,

$$\Delta L = (131)(4.1 \times 10^{-7} \times 1.11) \quad (2.12)$$

$$= 5.97 \times 10^{-5} \text{ m} \quad (2.13)$$

Next, assuming that the length change happens uniformly over 30 minutes, the rate of change of length of the fiber would be

$$\frac{dL}{dt} = \frac{5.97 \times 10^{-5}}{30 \times 60 \times 60} \quad (2.14)$$

$$= 5.53 \times 10^{-10} \text{ m/s} \quad (2.15)$$

Hence, the corresponding frequency of the temperature change would be

$$f = \frac{v}{\lambda} = \frac{5.53 \times 10^{-10}}{1550 \times 10^{-9}} \quad (2.16)$$

$$= 3.56 \times 10^{-4} \text{ Hz.} \quad (2.17)$$

2.5.3.2 Change in Refractive Index with Temperature

Another way that temperature changes can cause false detections in the setup is through the changes in refractive index of the fiber. The thermo-optic coefficient of silica is $8 \times 10^{-6}/^{\circ}\text{C}$

[49]. Following the same series of calculations,

$$\Delta n = (1.467)(8 \times 10^{-6} \times 1.11) \quad (2.18)$$

$$= 1.30 \times 10^{-5} \quad (2.19)$$

The rate of change of the refractive index of the fiber would then be

$$\frac{dn}{dt} = \frac{1.30 \times 10^{-5}}{30 \times 60 \times 60} \quad (2.20)$$

$$= 1.21 \times 10^{-10} \text{ /s} \quad (2.21)$$

which translates to the following rate of change of optical path

$$\frac{dL}{dt} = 2 \times (1.21 \times 10^{-10}) \times 131 \quad (2.22)$$

$$= 3.16 \times 10^{-8} \text{ m/s}, \quad (2.23)$$

using $\frac{dL}{dt} = 2L \frac{dn}{dt}$ [42]. Finally, the corresponding frequency of the temperature change would be

$$f = \frac{v}{\lambda} = \frac{3.16 \times 10^{-8}}{1550 \times 10^{-9}} \quad (2.24)$$

$$= 2.04 \times 10^{-2} \text{ Hz}. \quad (2.25)$$

In both cases, the frequency fluctuations due to the difference in temperature fluctuations are too small, at least 5 orders of magnitude lower than the detected frequencies in Figure 2.15. With this, we conclude that the detections were not due to the temperature fluctuations.

2.6 Why Michelson Interferometry

In this chapter, we have highlighted the development of a Michelson interferometer that is able to detect mechanical perturbations in both a lab and a building. Now that its working principles, as well as its application have been explained in detail, it is easier to understand why Michelson interferometry, and not other types, is chosen. There are many types of interferometers, with more popular examples being the Michelson interferometer, Mach-Zehnder interferometer and the Sagnac interferometer. While they each have their

own strengths, in the context of this thesis, Michelson interferometry would be the most advantageous.

Unlike Mach-Zehnder and Sagnac interferometry, Michelson interferometry requires only one submarine fiber as the sensing arm, while the reference arm can be a spool of fiber that remains on land. This is helpful as it allows for ease of length adjustments of the reference arm when attempting to equalise the length of the arms. It is unlikely that there are 2 submarine fibers which are equal in length, and even if they are, the other ends of the fibers may not be at the same place, and thus coupling them into the same beamsplitter would be a problem. With this in mind, employing the other forms of interferometry would require the use of an external cavity to minimise phase noise in the setup as a result of arm length difference of the order of kilometers. This is especially so because both arms in the other mentioned types of interferometry are required to be connected.

Additionally, employing Michelson interferometry allows us to control to polarisation states in the fibers easily, by simply connecting Faraday mirrors at the other terminals of the fibers. In Mach-Zehnder and Sagnac interferometry, since the sensing and reference arms are connected, the same cannot be applied. They would thus require additional components like polarisation controllers.

3 Converting into a Heterodyne Phasemeter

While it has been shown that the Michelson interferometer is able to detect perturbations, there is still room for improvement. Another limitation that the Michelson interferometer has is that it is unable to determine the direction of the measured displacement. Since the output power is sinusoidal, at the turning points the sensitivity to length goes to zero, and the direction of motion becomes ambiguous [36]. Referring to Figure 3.1, it can be seen that at the extreme points, e.g. the point indicated by the red ellipse, both positive and negative displacements would lead to a decrease in the signal amplitude.

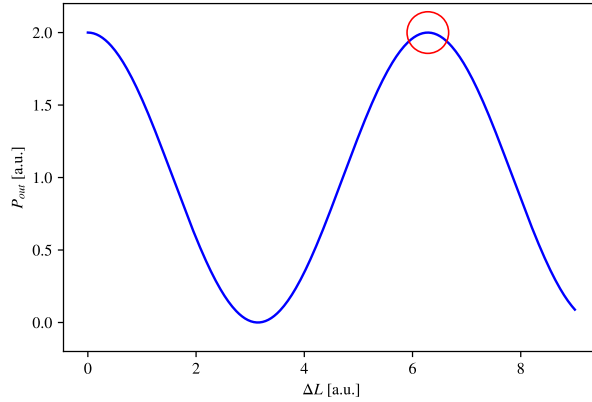


Figure 3.1: An ideal sinusoidal signal. At the extreme points (e.g. within the red ellipse), both increase and decrease in displacement leads to a decrease in signal amplitude. Hence, the direction of displacement is lost.

If we know the direction of displacement, we can then directly measure the differential phase ϕ_d instead of just its cosine value. This is important as the range of an *arccos* function is given by $[0, \pi]$. What this means is that if we were to try and unwrap the phase difference from the signal obtained using a Michelson interferometer, the obtained phase would be limited by that range, leading to discontinuities in the graph.

Hence, there is a need for a setup which enables us to extract direction so that we may obtain the exact phase changes induced in the presence of mechanical perturbations, and not just its cosine value. In this chapter, the conversion of the Michelson interferometer into a heterodyne phasemeter is described, along with its working principles and application.

3.1 Heterodyning the Setup

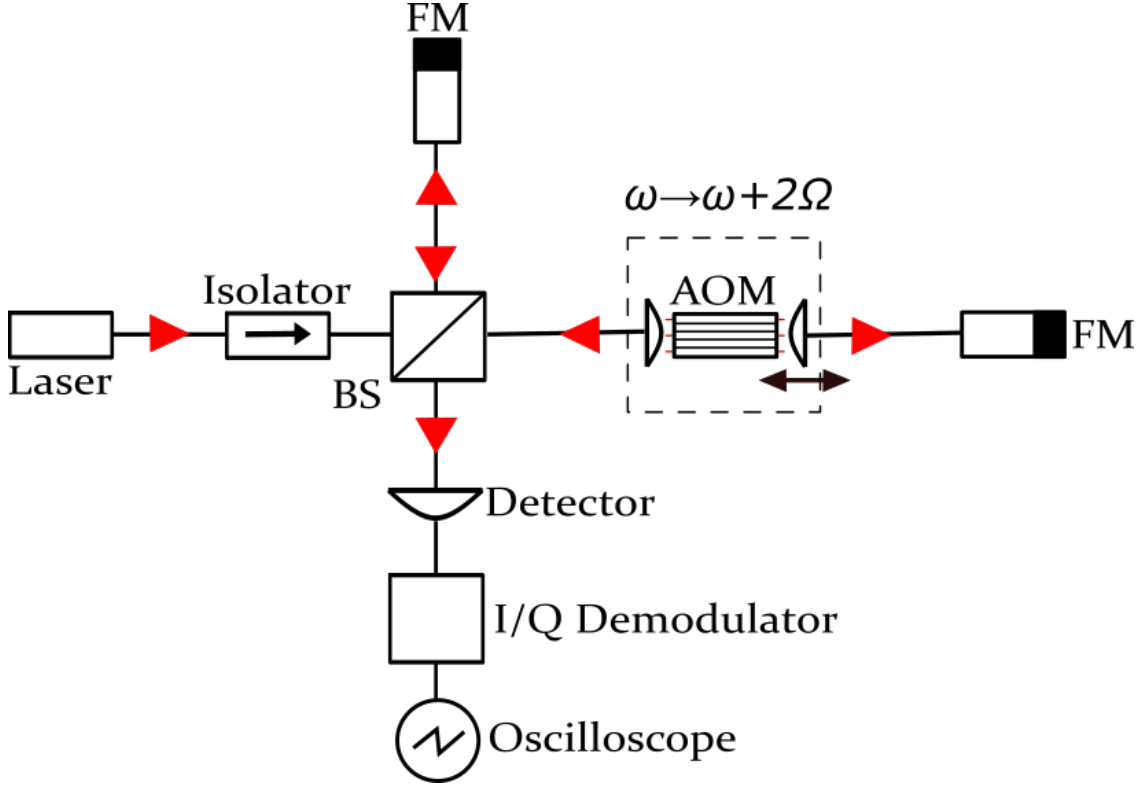


Figure 3.2: Heterodyne phasemeter setup. An acousto-optic modulator (AOM) is added in the reference arm to shift the frequency of laser by 2Ω . In the detection arm, I/Q demodulation is performed on the output signal from the photodiode.

The setup is similar to that of the Michelson interferometer, albeit with two main differences. First, there is an acousto-optic modulator (AOM) which shifts the laser frequency by a factor of Ω through the acousto-optic effect [50]. As the light beam passes through the AOM twice, the laser frequency will be shifted by 2Ω . For our case, $\Omega = 80$ MHz.

Now, when the light beams of 2 different frequencies recombine, the beams will pick up an additional phase corresponding to the difference in frequency, resulting in a beat-note.

$$E_{out} = \frac{1}{2} E_{in} e^{2ikL_x} (1 + e^{i(2\Omega t + \phi_d)}). \quad (3.1)$$

The output power of light incident on the photodiode, P_{out} is then calculated to be

$$P_{out} = \frac{P_{in}}{2} [1 + \cos(2\Omega t + \phi_d)]. \quad (3.2)$$

In the output port, the beat-note is then demodulated with both sine and cosine local oscillators through a process called *I/Q demodulation*, so that the changes in optical phase can be obtained unambiguously.

3.1.1 I/Q Demodulation

I/Q demodulation happens in the output port, after the detector. In Figure 3.2, the heterodyning components are simplified. The actual setup is shown in Figure 3.3.

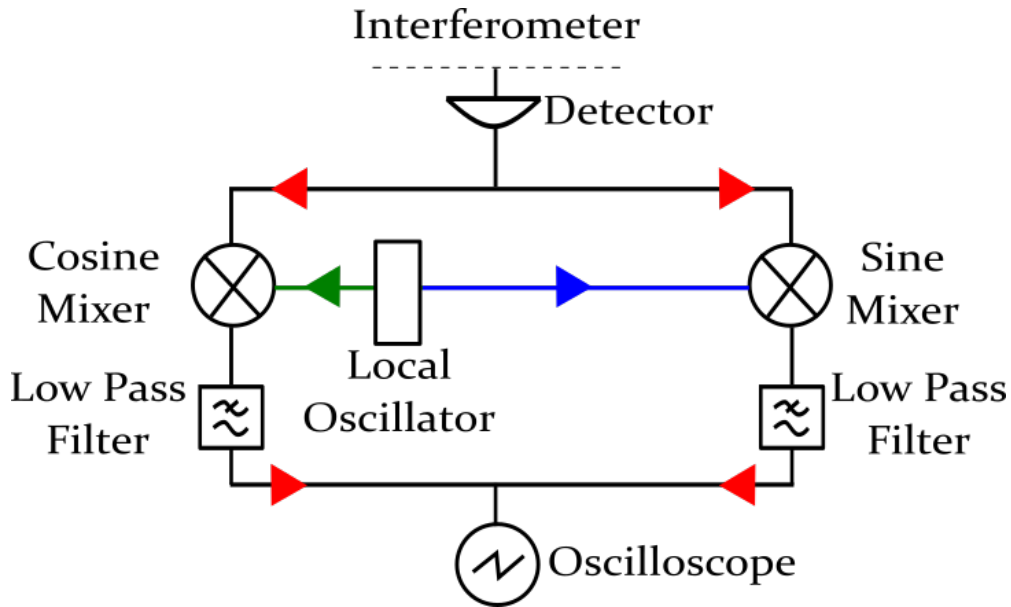


Figure 3.3: Close-up of the heterodyne component of the setup. The photodiode signal is split into two, and are each passed into different mixers. Likewise, the signal from a local oscillator is split, but through 2 fibers of different lengths, with a specified length difference. This delay would cause one of the local oscillator signal to be out of phase by a factor of $\pi/2$. After the mixers, the signals are then passed through low-pass filters, before being analyzed at the oscilloscope.

The local oscillator in our case comes from a direct digital synthesis (DDS), which is split into two fibers. The two fibers are selected such that the length difference between them would cause one signal to be out of phase by the other by $\pi/2$. The in-phase signal is termed as the *I* signal, while the out-of-phase signal is termed as the *Q* signal, hence the name of this technique.

This required length difference can be found by using the equation

$$v = f\lambda, \quad (3.3)$$

or specifically,

$$\frac{\lambda}{4} = \frac{v}{4f} \quad (3.4)$$

where v is the speed of light in the fiber, f is the frequency of the signal and λ is the wavelength. Equation 3.3 can be rearranged into Equation 3.4, resulting in a form which explicitly gives the required length difference. With $f = 160$ MHz and $v = (0.659)(3 \times 10^8)$ m/s,

$$\frac{\lambda}{4} = 0.3125 \text{ m.} \quad (3.5)$$

The speed of light was multiplied by a velocity factor of 0.659 to account for the refractive index of the fiber. With this information, the 2 fibers were then chosen such that they have a length difference of about 30 cm, and with this we have our sine and cosine local oscillators.

The signal from the photodiode is split into two and then mixed with the local oscillators. For the I term, it is demodulated with a cosine

$$I = \frac{P_{in}}{2}(1 + \cos(2\Omega t + \phi_d)) \cos(2\Omega t) \quad (3.6)$$

$$= \frac{P_{in}}{2}[2 \cos(2\Omega t) + \cos(4\Omega t + \phi_d) + \cos(\phi_d)]. \quad (3.7)$$

On the other hand, the Q term is demodulated with a sine

$$Q = \frac{P_{in}}{2}(1 + \cos(2\Omega t + \phi_d)) \sin(2\Omega t) \quad (3.8)$$

$$= \frac{P_{in}}{2}[2 \sin(2\Omega t) + \sin(4\Omega t + \phi_d) - \sin(\phi_d)]. \quad (3.9)$$

These quadrature signals are then passed through low pass filters, where all terms with multiples of $2\Omega t$ are eliminated. This leaves only the final term containing the differential phase ϕ_d

$$I = \frac{P_{in}}{2} \cos(\phi_d) \quad (3.10)$$

$$Q = -\frac{P_{in}}{2} \sin(\phi_d). \quad (3.11)$$

The optical phase can then be unambiguously extracted over many wavelengths. An

example of a readout of the heterodyne phasemeter when a perturbation (a tap on the table in this case) is detected is shown in Figure 3.4.

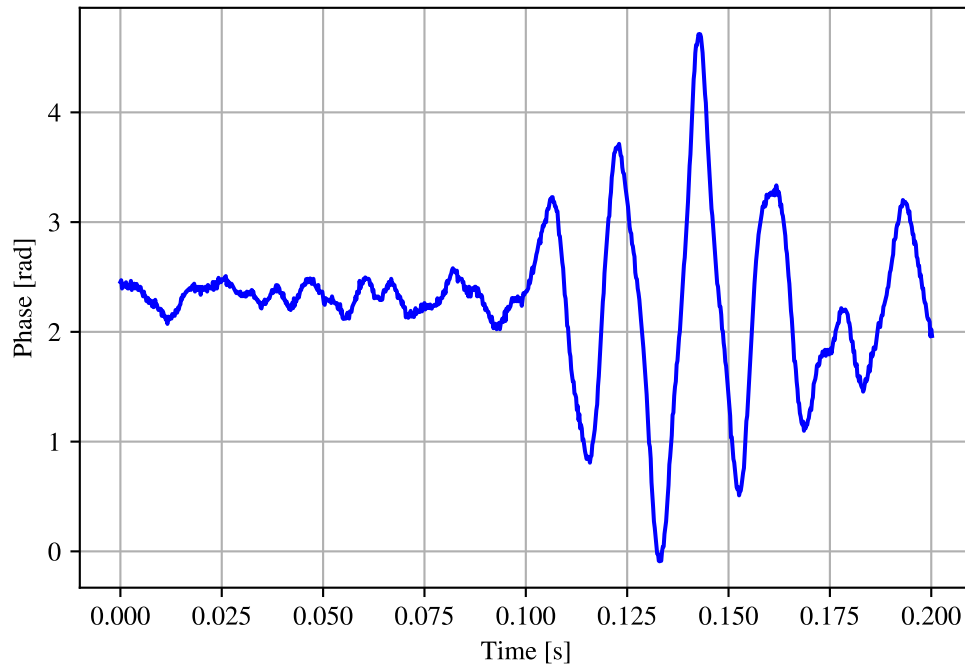


Figure 3.4: Phase fluctuations unwrapped through I/Q demodulation, induced by tapping on the table.

3.2 Perturbation Sensing in Lab

As a test, the oscilloscope is set to save waveforms continuously for a period of over a minute. I/Q demodulation is then performed after data collection, and the results are shown in Figure 3.5.

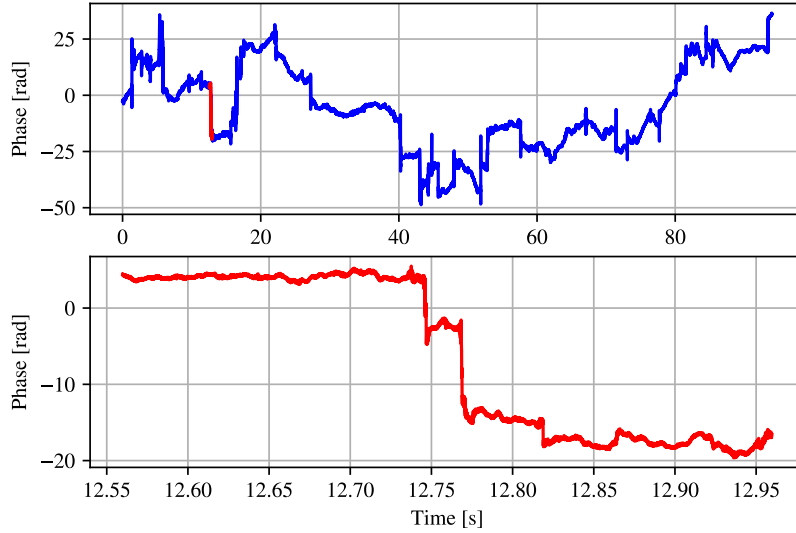


Figure 3.5: Phase changes for a period over a minute. Data was collected in the lab at 4 pm, on 24 March 2021. The bottom graph is subset of the top graph (indicated by the red portion).

At first glance, the sudden dips and increases in the graph seem to indicate that there are discontinuities, which would mean that the phase unwrapping process is not done correctly. Discontinuities happen when the perturbation is large - large enough to cause the measured phase to jump by more than π within one time step. However, this is not the case. In the bottom graph of Figure 3.5, the maximum phase difference between consecutive data points is found to be 0.432. This means that the sampling rate that was used here (50,000 samples per second) is appropriate.

Another way to check if the results make sense is to estimate the speed of the induced perturbation. Consider the same highlighted period in Figure 3.5. The drop in measured phase is about 25 rad, and it happened within approximately 50 ms. Using $\phi_d = 2k\Delta L$, we can thus determine the speed of the perturbation,

$$\frac{dL}{dt} = \frac{1}{2k} \frac{d\phi_d}{dt} \quad (3.12)$$

$$= \frac{1550 \times 10^{-9}}{4\pi} \left(\frac{-25}{50 \times 10^{-3}} \right) \quad (3.13)$$

$$\approx 0.609 \text{ mm/s}, \quad (3.14)$$

which is a reasonable value.

4 Conclusion and Outlook

The thesis described the development of a fiber-based interferometric system capable of detecting perturbations in the environment. When the fibers are perturbed, the heterodyne phasemeter is able to measure and read out the changes in optical phase without any direction ambiguity. Its design and instrumentation is largely based on the basic principles of Michelson interferometry.

The importance of having global coverage of seismic sensors was introduced in Chapter 1, which motivates our choice of developing a fiber-based interferometer. Existing submarine fibers offer an attractive option to seismic detection mainly because they have already been installed in abundance [31]. Connecting them into the arms of an interferometer is therefore a cost-effective alternative, as compared to deploying more OBSs in the ocean [26, 29, 30].

The choice of Michelson interferometry, as well as its principles, were briefly discussed in Chapter 2. While there are various types of interferometry, Michelson interferometry identifies as the most suitable, when considering the cost and complexity of the would-be setup. In the same chapter, the construction and implementation of the Michelson interferometer were highlighted in detail. Due to the prevalence of phase noise, having equal paths is a necessity which can be achieved by the photon coincidence method. Perturbation sensing was done in the lab and building, producing results that agree with our initial expectations.

The problem of direction ambiguity was tackled in Chapter 3, where the Michelson interferometer was converted into the heterodyne phasemeter. This was done by heterodyning the setup in which I/Q demodulation can be performed to obtain the readout of phase changes in the fibers. A short test was carried out in the lab, and with a simple analysis, we concluded that the obtained results were reasonable.

Moving forward, larger scales of tests should be run with the heterodyne phasemeter. For example, the next step could be attempting to sense perturbations in the building. In the context of using fibers to detect earthquakes, special care should be taken to limit the difference in temperature fluctuations in the two environments. The reason for this is that the calculated frequency of changes in refractive index due to temperature coincide with that of an earthquake's. That aside, future efforts could also be focused on making the setup more compact. The existing state of the heterodyne phasemeters uses a lot of fibers.

Tendency to mess aside, this makes the setup more susceptible to unwanted noise in the environment.

Bibliography

- [1] Hannah Ritchie and Max Roser. Natural disasters. *Our World in Data*, 2014. <https://ourworldindata.org/natural-disasters>.
- [2] Michel Masozera, Melissa Bailey, and Charles Kerchner. Distribution of impacts of natural disasters across income groups: A case study of new orleans. *Ecological Economics*, 63(2):299–306, 2007. Ecological Economics of Coastal Disasters.
- [3] United Nations Office for Disarmament Affairs. *Human Cost of Disasters*. United Nations, 2020.
- [4] Prema chandra Athukorala. Disaster, Generosity and Recovery: Indian Ocean Tsunami. Departmental Working Papers 2012-04, The Australian National University, Arndt-Corden Department of Economics, April 2012.
- [5] Rohan Best and Paul J Burke. Macroeconomic impacts of the 2010 earthquake in Haiti. Departmental Working Papers 2017-15, The Australian National University, Arndt-Corden Department of Economics, December 2017.
- [6] Huicong Jia, Fang Chen, Donghua Pan, and Chuanrong Zhang. The impact of earthquake on poverty: Learning from the 12 may 2008 wenchuan earthquake. *Sustainability*, 10:4704, December 2018.
- [7] Ahmad J. Durrani, A. Elnashai, Y. Hashash, S. Kim, and A. Masud. The kashmir earthquake of october 8, 2005 : a quick look report. December 2005.
- [8] T. G. Sitharam, Naveen James, and Sreevalsa Kolathayar. *Earthquake and Seismicity*, pages 11–31. Springer International Publishing, Cham, 2018.
- [9] John F. Cassidy. *Earthquake*, pages 208–223. Springer Netherlands, Dordrecht, 2013.
- [10] Xianyun Wu and Ru-Shan Wu. *Seismic Wave Propagation*, pages 1535–1544. Springer New York, New York, NY, 2008.
- [11] Peter M. Shearer. *Introduction to Seismology*. Cambridge University Press, 2 edition, 2009.
- [12] David M. Boore. The richter scale: its development and use for determining earthquake source parameters. *Tectonophysics*, 166(1):1–14, 1989. Quantification of Earthquakes and the Determination of Source Parameters.
- [13] Peter Bormann and Domenico Giacomo. The moment magnitude and the energy magnitude : common roots and differences. *Journal of Seismology*, 15(2):411–427,

December 2010.

- [14] Zakeria Shnizai. The haiti earthquake on 12 th of january 2010 destroyed the city of port-au-prince. scientist knew that a major earthquake was likely in the region, and that building construction standards were low, and yet measures were not taken to mitigate this 'natural disaster. May 2011.
- [15] G. Purcaru. The Great Sichuan Earthquake of May 12, 2008 (Mw7.9) - An Unpredictable Earthquake. In *AGU Fall Meeting Abstracts*, volume 2008, pages S31B-1919, December 2008.
- [16] Jennifer Parker Hamilton and Sarah J. Halvorson. The 2005 Kashmir Earthquake. *Mountain Research and Development*, 27(4):296 – 301, 2007.
- [17] Costas E. Synolakis and Laura Kong. Runup measurements of the december 2004 indian ocean tsunami. *Earthquake Spectra*, 22(3_suppl):67-91, 2006.
- [18] Emma Marris. Inadequate warning system left asia at the mercy of tsunami. *Nature*, 433:3-5, February 2005.
- [19] Anawat Suppasri, Kazuhisa Goto, Abdul Muhari, Prasanthi Ranasinghe, Mahmood Riyaz, Muzailin Affan, Erick Mas, Mari Yasuda, and Fumihiko Imamura. A decade after the 2004 indian ocean tsunami: The progress in disaster preparedness and future challenges in indonesia, sri lanka, thailand and the maldives. December 2015.
- [20] Nabeel Ahmad, Shahid Riaz, Muhammad Awais, Zeeshan Jilani, Nora Ahmad, Irfan, Javeed, Aftab Alam, and Mahmood Sultan. Earthquake prediction: A global review and local research. *Pakistan academy of Sciences* 46(4):233-246.2009, January 2009.
- [21] Thorne Lay and Terry C. Wallace. Chapter 5 - seismometry. In *Modern Global Seismology*, volume 58 of *International Geophysics*, pages 173-199. Academic Press, 1995.
- [22] A T Ringler, J Steim, D C Wilson, R Widmer-Schmidrig, and R E Anthony. Improvements in seismic resolution and current limitations in the Global Seismographic Network. *Geophysical Journal International*, 220(1):508-521, October 2019.
- [23] Jordi Diaz, Martin Schimmel, Mario Ruiz, and Ramon Carbonell. Seismometers within cities: A tool to connect earth sciences and society. *Frontiers in Earth Science*, 8:9, 2020.
- [24] Mahmoud Mohamed Selim Saleh. *Body Waves*, pages 29-35. Springer Netherlands, Dordrecht, 2011.

- [25] Arthur D. Frankel. How does the ground shake? *Science*, 283(5410):2032–2033, 1999.
- [26] Giuseppe Marra, Cecilia Clivati, R. Lockett, Anna Tampellini, Jochen Kronjaeger, Louise Wright, Alberto Mura, Filippo Levi, Stephen Robinson, André Xuereb, Brian Baptie, and Davide Calonico. Ultrastable laser interferometry for earthquake detection with terrestrial and submarine cables. *Science*, 361:eaat4458, June 2018.
- [27] Fujiwara Noriyuki, Hishiki Kenji, and Katayama Takeshi. Ocean-bottom seismographic observation systems. 2010.
- [28] Barbara Romanowicz, D. Stakes, D. Dolenc, Doug Neuhauser, Paul McGill, R. Uhrhammer, and Tatiana Ramirez. The monterey bay broadband ocean bottom seismic observatory. *Annals of Geophysics*, 49, April 2006.
- [29] Antony Joseph. Chapter 10 - earthquake monitoring for early tsunami warnings. In Antony Joseph, editor, *Tsunamis*, pages 125–148. Academic Press, Boston, 2011.
- [30] Alex Lopatka. Deploying seismometers where they’re needed most: Underwater. *Physics Today*, May 2019.
- [31] P. Gabla, E. Handa, B. Burns, R. Wopschall, E. Contag, I. Douglas, J. Hibbard, J. Levine, L. Cook, J. Rawle, H. Souisa, and W. Nielsen. Submarine telecoms industry report. October 2016.
- [32] Z. W. Zhan, M. Cantono, V. Kamalov, A. Mecozzi, R. Müller, S. Yin, and J. C. Castellanos. Optical polarization-based seismic and water wave sensing on transoceanic cables. *Science*, 371(6532):931–936, 2021.
- [33] N. J. Lindsey, E. R. Martin, D. S. Dreger, B. Freifeld, S. Cole, S. R. James, B. L. Biondi, and J. B. Ajo-Franklin. Fiber-optic network observations of earthquake wavefields. *Geophysical Research Letters*, 44(23):11,792–11,799, 2017.
- [34] J. Mestayer, B. Cox, P. Wills, D. Kiyashchenko, J. Lopez, M. Costello, S. Bourne, G. Ugueto, R. Lupton, G. Solano, D. Hill, and A. Lewis. *Field Trials of Distributed Acoustic Sensing for Geophysical Monitoring*, pages 4253–4257. 2012.
- [35] F. Zujie, K. Chin, R. Qu, and H. Cai. *Fundamentals of Optical Fiber Sensors*. August 2012.
- [36] J. Watchi, S. Cooper, B. Ding, C. M. Mow-Lowry, and C. Collette. A review of compact interferometers. *Review of Scientific Instruments*, 89(12), 2018.
- [37] L. Bonino, F. Bresciani, G. Piasini, M. Pisani, A. Cabral, J. Rebordão, and F. Musso. An Interferometer for High-resolution Optical Surveillance from GEO - Internal Metrology

- Breadboard. In *International Conference on Space Optics — ICSSO 2006*, volume 10567, pages 744–750. SPIE, 2017.
- [38] C. Zhu, Y. Chen, Y. Du, Y. Zhuang, F. Liu, R. Gerald, and J. Huang. A displacement sensor with centimeter dynamic range and submicrometer resolution based on an optical interferometer. *IEEE Sensors Journal*, July 2017.
- [39] F. E. Seraji and G. Toutian. Effect of temperature rise and hydrostatic pressure on microbending loss and refractive index change in double-coated optical fiber. *Progress in Quantum Electronics*, 30(6):317–331, 2006.
- [40] A. Dandridge and A. B. Tveten. Phase noise of single-mode diode lasers in interferometer systems. *Applied Physics Letters*, 39(7):530–532, 1981.
- [41] Emil Wolf. *Introduction to the theory of coherence and polarization of light*. Cambridge Univ. Press, Cambridge, 2007.
- [42] Mark Fox. *Quantum Optics: An Introduction*. Oxford Master Series in Atomic, Optical, and Laser Physics. Oxford University Press, 2006.
- [43] Y. Tamura, H. Sakuma, K. Morita, M. Suzuki, Y. Yamamoto, K. Shimada, Y. Honma, K. Sohma, T. Fujii, and T. Hasegawa. The first 0.14-dB/km loss optical fiber and its impact on submarine transmission. *Journal of Lightwave Technology*, 36(1):44–49, 2018.
- [44] K. Stubkjaer and M. Small. Noise properties of semiconductor lasers due to optical feedback. *IEEE Journal of Quantum Electronics*, 20(5):472–478, 1984.
- [45] P. Drexler and P. Fiala. Utilization of faraday mirror in fiber optic current sensors. *Radio Engineering*, 17, January 2008.
- [46] E. M. Yousif. The faraday effect explained. *IOSR Journal of Applied Physics*, 9, September 2017.
- [47] M. Legré, R. Thew, H. Zbinden, and N. Gisin. High resolution optical time domain reflectometer based on 1.55 μm up-conversion photon-counting module. *Optical Society of America*, 2007.
- [48] X. Li, S. Lin, J. Liang, Y. Zhang, H. Oigawa, and T. Ueda. Fiber-optic temperature sensor based on difference of thermal expansion coefficient between fused silica and metallic materials. *IEEE Photonics Journal*, 4:155–162, February 2012.
- [49] D. Fernandes, R. Winter, J. C. Silva, R. Kamikawachi, and A. Macedo. Influence of temperature on the refractive index sensitivities of fiber bragg gratings refractometers. *Journal of Microwaves, Optoelectronics and Electromagnetic Applications*, 16, April

2017.

- [50] J. Barrios, J. Álvarez, and F. J. Racedo. Characterization and optimization of the laser diffracted by an acoustic-optical modulator in the infrared region. *Journal of Physics: Conference Series*, 1219, May 2019.